Smart Morphable Surfaces for Aerodynamic Drag Control

Denis Terwagne, Miha Brojan, and Pedro M. Reis*

Engineering the topography of surfaces can offer augmented functionality.[1–4] As a canonical example, the nano-texture on the streamlined bodies of sharks can decrease their skin friction drag and improve swimming performance.[5] For a blunt object, texturing can also reduce drag, albeit through a different mechanism that arises from the flow separating from the surface. For instance, some cactus trees (*Carnegia gigantean*) can resist uprooting under high winds due to surface grooves[6] and dimples on a golf ball increase its 'carry distance'.[7,8] Active mechanisms have been developed to control this form drag,[9–12] but typically involve elementary surface units that are impractical for large areas. Here, we devise a new class of Smart Morphable Surfaces, which we refer to as Smorphs, that make use of a wrinkling instability on curved surfaces to generate custom, switchable and tunable topography. Our experiments show that surface curvature qualitatively affects the wrinkled pattern, when compared to flat film-substrate systems.[13–16] Inspired by the resemblance of our dimpled patterns and those of golf balls, we have characterized their aerodynamic performance and found that the drag coefficient can be reduced, on demand, by up to a factor of two.

The dimpled pattern of a golf ball induces a laminar-to-turbulent transition in the boundary layer that envelopes part of their surface and delays of the point of separation between forward and reverse flow. This reduces the size of the downstream wake and, consequently, lowers the aerodynamic drag by as much as a factor of two, when compared to a smooth sphere counterpart.[7,8,18,19] A drawback of this mechanism with static dimples is that a fixed surface morphology may not always be aerodynamically favorable. According to Achenbach's seminal work,[19,20] a rough surface triggers an early laminar-to-turbulent transition, decreasing drag, but can become disadvantageous when the flow speed is further increased. Recent efforts in engineering active surfaces to control the flow past a structure include electro-mechanical transducers,[9,10] plasma actuators[11] and electro-active polymers.[12] However, most of these mechanisms involve actuation of elementary surface units and

are often impractical to implement over the large areas required for aerodynamic applications.

In our experiments, we employ rapid prototyping to fabricate spherical specimens comprising a thin-stiff outer shell adhered to a softer substrate core, which contains an under-surface cavity of radius R_o (**Figure 1**a and 1b). More details on the fabrication process of the samples and the materials used are provided in the Supporting Information. The design parameters lie within the ranges: radius of sample, $9.5 \leq R[\text{mm}] \leq 20$ ($R_o/R = 0.45$), thickness of shell, $20 \leq h[\mu\text{m}] \leq 1000$, ratio of Young's moduli, $9 \leq E_f/E_s \leq 162$, and Poisson's ratios, $\nu_f = \nu_s = 0.5$, for the shell (E_f, ν_f) and substrate (E_s, ν_s), respectively. The cavity is connected to a pneumatic system that sets a pressure differential, $\Delta P = P_e - P_i$, between the internal, P_i, and external (atmospheric), P_e, pressures of the sample. Upon depressurization (increasing ΔP), the structure is placed under homogeneous compression, which excites an undulatory wrinkled morphology from what was originally a smooth shell (Figure 1a and 1b).

The resemblance between some of our observed patterns and the dimples on a golf ball has motivated us to explore their usage for aerodynamic drag reduction. The added novelty of pneumatic control, however, is that it allows for dynamic switching and tuning of the mechanism, which is systematically characterized through wind tunnel tests (Figure 1c). The fast responsiveness and reversibility of our mechanism are significant advantages when contrasted with other possible forms of actuation, e.g., through thermal expansion[13] or swelling.[21] Furthermore, exploiting a mechanical instability to self-organize surface patterns facilitates implementation over large areas.

We start by contrasting the wrinkling of our spherical shell-substrate Smorphs to the more prevalent flat plate-substrate systems,[13,15,22] whose characteristic wrinkling wavelength is given by,[14,16]

$$\lambda_{th}^{flat} = 2\pi h \left(\frac{E_f\left(1-\nu_s^2\right)}{3E_s\left(1-\nu_f^2\right)} \right)^{\frac{1}{3}} \tag{1}$$

for the film and substrate parameters defined above. Under biaxial loading conditions, the possible solutions include checkerboard, hexagonal, herringbone and labyrinthine patterns.[13,15,16] However, the hexagonal (dimpled) pattern can only be stabilized in a limited region of parameter space,[23] due to their typical higher energetic cost. Also, it has been suggested that adding a small degree of curvature to the substrate can help stabilize hexagonal patterns but the underlying mechanism remains quantitatively unclear.[23]

Towards investigating the effect of curvature of the substrate on the wrinkling morphology, we characterize our experimental patterns and quantify their characteristic length scales. In **Figure 2**a, we present the phase diagram of our system, where we superpose data for different values of R, as a function of the ratios of Young Moduli, E_f/E_s, and the sample radius to

D. Terwagne,[+] M. Brojan,[†] P. M. Reis
Department of Civil and Environmental Engineering
Massachusetts Institute of Technology
Cambridge, MA 02139, USA
E-mail: preis@mit.edu

P. M. Reis
Department of Mechanical Engineering
Massachusetts Institute of Technology
Cambridge, MA 02139, USA

[+]Current address: Faculté des Sciences, Université Libre de Bruxelles (ULB), Bruxelles 1050, Belgium
[†]Current address: Faculty of Mechanical Engineering, University of Ljubljana, Slovenia
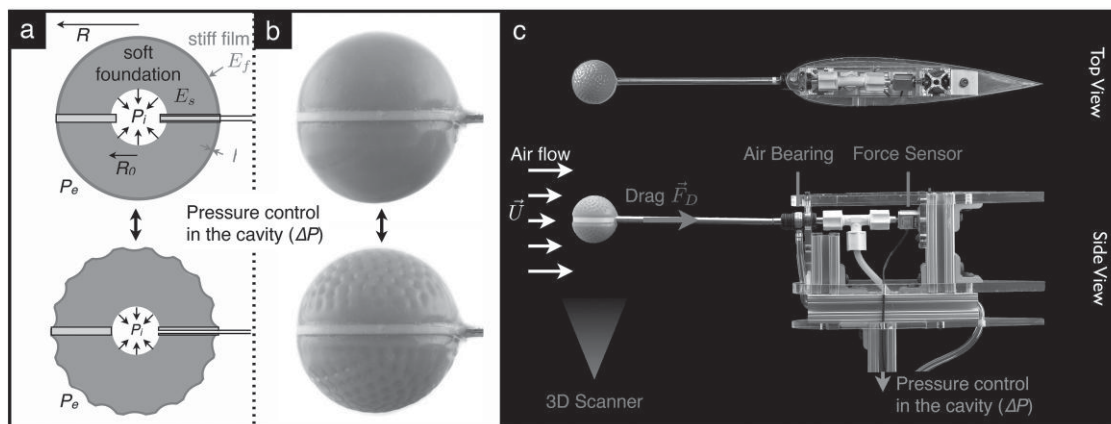
Figure 1. Experimental samples and apparatus for wind tunnel testing. a, Schematic of the pressure-driven wrinkling process of our spherical Smorphs. The smooth (top) and wrinkled (bottom) configurations correspond to low and high levels of depressurization, ΔP, respectively. b, Experimental counterparts. Two hemispherical samples (radius, $R = 20$ mm) consisting of a thin stiff film (thickness $h = 510$ µm, Young modulus, $E_f = 2100$ kPa) surrounding a softer core foundation (modulus, $E_s = 230$ kPa) and a cavity (radius, $R_o = 9$ mm) are assembled around a rigid annulus at their equator. A rigid pipe connects the cavity to a vacuum pump for depressurization (top Smorphs, $\Delta P < 5$ kPa; bottom Smorphs, $\Delta P = 50$ kPa). The resulting wavelength is $\lambda = 4.37 \pm 0.25$ mm. c, Custom designed load cell for wind tunnel testing (see Supporting Information).

shell thickness, R/h. For $R/h < 10^2$, there is an extended region where hexagonal-like dimples are observed. Labyrinthine patterns are found for $R/h > 10^2$. In the vicinity of $R/h \sim 10^2$, hybrids of dimples and labyrinths occur. Some of our samples (Figure 2a, crossed symbols) are already pre-wrinkled at rest, especially those with thinner shells in the labyrinthine region; presumably due to the residual stresses induced by the irreversible swelling of PDMS during fabrication. For all others, the wrinkling pattern emerges from an originally smooth surface. The fact that we observe different patterns as a function of R/h indicates that the curvature of the substrate does indeed have a strong qualitative effect on the selection of the wrinkling mode, as it stabilizes the dimpled pattern that is otherwise energetically unfavorable on the flat substrate counterpart.[23] This is consistent with the recent work,[21,24,25] albeit with our different

driving mechanism and the ability to finely target the geometric and material properties of the system.

We proceed by attesting whether the curvature of the substrate also affects the wrinkling length scale. Using digital imaging, we measure the wavelength, λ_{exp}^R, of both labyrinthine and dimpled patterns (schematic in Figure 2b) for hemispherical samples with a range of values for R, h, and E_f/E_s. In Figure 2b, we plot λ_{exp}^R versus the theoretical prediction for a flat substrate, λ_{th}^{flat}, from Equation (1). We find that all the experimental data collapse onto a line with unit slope, indicating that the curvature of the substrate (at least in the range of R explored) leaves λ_{th}^{flat} unchanged. Curvature does, however, affect the mode of the selected pattern, as mentioned above.

Profilometry through three-dimensional laser scanning (Supporting Information and Figure S2) is employed to
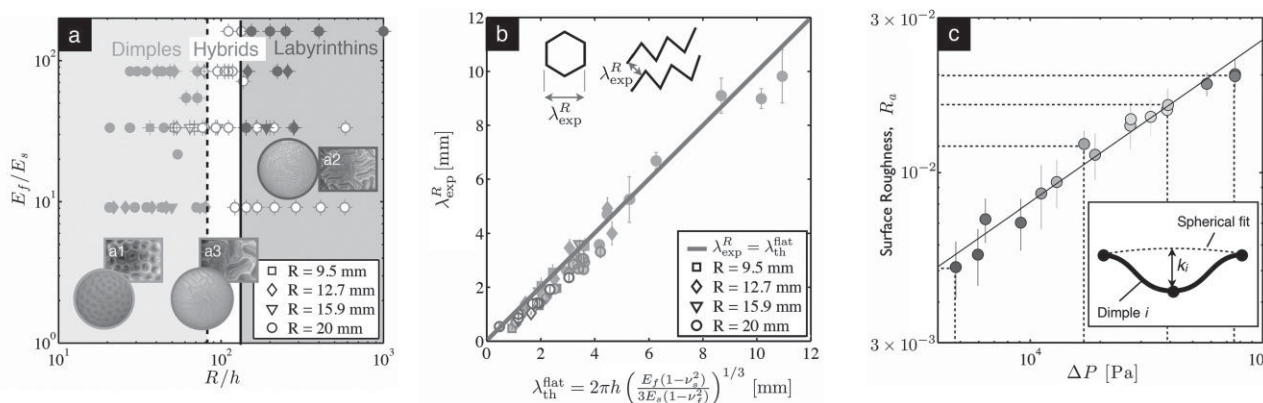

Figure 2. Characterization of the wrinkling morphologies. a, Phase diagram of the wrinkling patterns at onset for samples of different geometric (R,h) and material (E_f,E_s) properties: Dimples (inset a1 and orange solid symbols), Labyrinths (inset a2 and blue solid symbols) and Hybrids of dimples and labyrinths (inset a3 and white-filled symbols). Symbols marked with a central cross correspond to samples that were pre-wrinkled upon fabrication. b, Experimental measurements of the wrinkling wavelength of the curved experimental samples vs. the theoretical prediction for the flat case, Equation (1) in the text. The solid line has unit slope. c, Surface roughness, R_a, (measurement described in Supporting Information), as a function of the level of depressurization, ΔP, for the same sample tested and described in Figure 1a. The solid line is the power-law, $R_a \sim \Delta P^{0.5}$. The four different values of the roughness tested in the wind tunnel (used in Figure 3a) are highlighted using dashed lines.

further quantity the surface topography by the depth, k_i, of each dimple and labyrinthine valley (schematic in Figure 2c). The average surface roughness for n dimples can then be calculated, $R_a = 1/n \sum_{i=1}^{n} |k_i/2R|$, as defined in classic aerodynamic studies.[19,20] In Figure 2c we plot R_a versus differential pressure, ΔP, for the sample discussed above, in Figure 1a. The surface roughness is found to increase monotonically with ΔP, consistently with a power law, $R_\alpha \sim \Delta P^\alpha$, with $\alpha \simeq 0.5$ (Figure 2c, solid line). By tuning ΔP, we can therefore target specific values of the surface roughness on demand.

We now turn to exploring the aerodynamic performance of our switchable and tunable Smorphs. In Figure 1c, we presented a photograph of the apparatus used for wind tunnel testing (Supporting Information); two identical hemispherical samples are assembled, mounted onto a load cell and coupled to a pneumatic system. Emphasis is given to samples that exhibit dimpled patterns, given their resemblance to golf balls. We chose to test a sample with a wrinkling wavelength, $\lambda = 4.37 \pm 0.25$ mm, which is comparable to the dimple size common in golf ball designs. By increasing ΔP, the average dimple depth can be varied over the range $0 \le \langle k_i \rangle [\mathrm{mm}] \le 0.8$, i.e., a surface roughness in the range $0 < R_a < 0.02$. The sample is loaded in the wind tunnel with a laminar flow at Reynolds number, $Re = \frac{\rho_a U(2R)}{\mu_a}$, in the range $3 \times 10^4 < Re < 12 \times 10^4$, where U is the flow speed and, ρ_a and μ_a are the density and the dynamic viscosity of air, respectively. The resulting aerodynamic drag force, F_D, along the axis of the flow, is then measured (Supporting Information). Consequently, the drag coefficient is calculated as, $C_D = \frac{2F_D}{\rho_a U^2 \pi R^2}$.

In **Figure 3**a we plot the drag coefficient, C_D, as a function of the Reynolds number, at different levels of surface roughness, R_a. When the sample is nearly smooth (e.g., $R_a = 490 \times 10^{-5}$), we observe an approximately constant $C_D \sim 0.5$, which is indicative of a laminar boundary layer around the sphere. Increasing the surface roughness results in C_D decreasing steeply past a critical value of Reynolds number, Re_c. This process is often referred to as drag crisis,[18,26] and corresponds to a laminar-to-turbulent transition in the boundary layer near the surface. As the depth of the dimples is progressively increased (e.g. curves with $R_a = \{1180, 1510, 1950\} \times 10^{-5}$ in Figure 3a, the drag crisis occurs for lower values of Re_c. Our findings are in agreement with the seminal work of Achenbach's[18–20] for spheres and cylinders with different roughness, albeit with a surface topography that we can actively tune.

Testing samples with a labyrinthine pattern ($R_a = 900 \times 10^{-5}$, squares in Figure 3a), resulted in a significant increase of the C_D, past Re_c, whereas for the roughest dimpled sample ($R_a = 1950 \times 10^{-5}$, Figure 3a), we found a post-critical plateau for C_D. The aerodynamic advantage of periodic tiled patterns was first suggested by Bearman and Harvey,[7] who compared measurements of the drag coefficient on golf balls to spheres and cylinders with random roughness.[19,20] The post-critical increase of C_D for random topographies, in contrast to the plateau for periodic tilings, was attributed to an anomalous thickening of the turbulent boundary layer,[27] which facilitates separation, and is well aligned with our results.
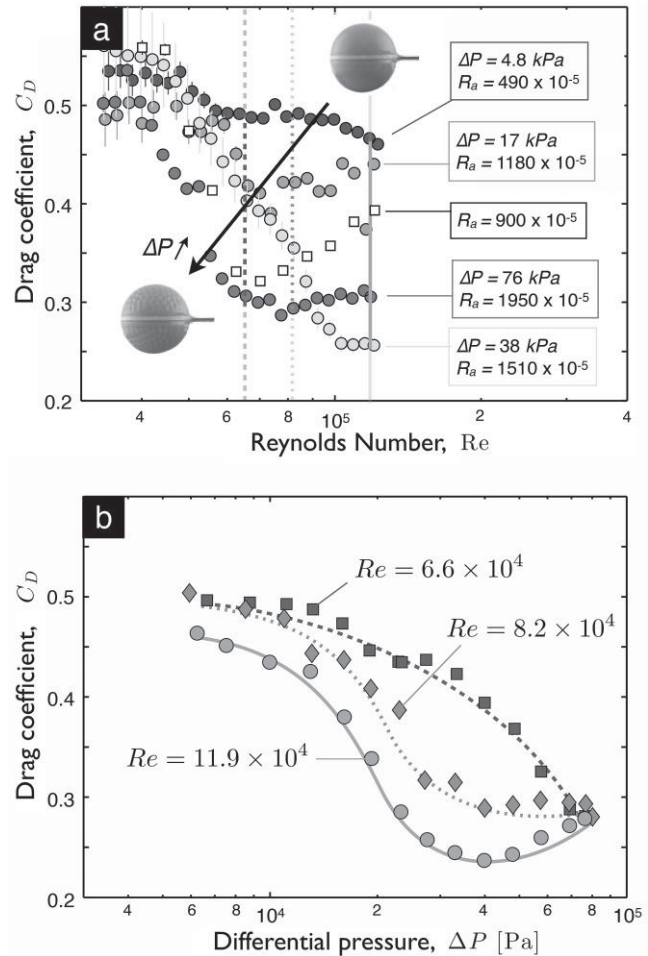

Figure 3. Aerodynamic performance of Smorphs. a, Drag coefficient, C_D, vs. Reynolds number, Re, for different level of depressurization of the same dimpled sample described in Figure 1a (circles). The roughness parameter, R_a, and level of depressurization, ΔP, are indicated next to each curve. For comparison, a curve for a labyrinthine pattern of roughness, $R_a = 900 \times 10^{-5}$, is represented by squares. b, Drag coefficient, C_D, as a function of the depressurization, ΔP, for three different values of Reynolds number: $Re = 6.6$, 8.2 and 11.9×10^4. Lines are guides to the eye. The corresponding values of Re were indicated in Figure 3a by the vertical dashed, dotted and solid lines.

The tunability of our drag reduction mechanism is further illustrated in Figure 3b where we plot the drag coefficient, C_D, of the dimpled Smorphs as a function of ΔP, for three specific values of the Reynolds number ($Re = \{6.6, 8.2, 11.9\} \times 10^4$). The continuous variation of C_D vs. ΔP demonstrates the ability for drag on our Smorphs to be precisely controlled by a single pressure signal. Moreover, whereas C_D decreases monotonically for the two lowest values of Re, the behavior is non-monotonic at high values of Re. This suggests that optimal configurations for minimum drag can be attained through precise tuning of the surface roughness, R_a, depending on the flow conditions set by Re. This finding is further emphasized through the results in Figure 3a (at $Re = 9 \times 10^4$), where the drag curve for $R_a = 1510 \times 10^{-5}$ crosses that for $R_a = 1950 \times 10^{-5}$. This crossover indicates that deep dimples are not always advantageous for drag reduction at all values of the Reynolds number and, eventually,

COMMUNICATION

a smooth sphere has the lowest drag coefficient.[19,28] Dimples can, therefore, have competing effects: if too shallow, they do not effectively trigger the drag crisis in the range $10^4 < Re < 10^6$; if too deep, they increase drag by thickening the boundary layer at higher Re. These findings should motivate future studies on the optimization of our switchable and tunable mechanism and call for an analysis of the effect of dimple geometries on the boundary layer flow.

We envision that our switchable and tunable Smorphs could find applications in a variety of aerodynamic structures. A particularly novel aspect of our Smorphs is that complex topography can be rapidly activated with a single pressure signal and their actuation speed is only limited by how fast the depressurization can be set. The fast elastic response of our mechanism opens the possibility of on demand and dynamic drag control. Focus was given to the specific case of a bluff body, taking a spherical configuration as a proof of concept. However, Smorphs could also be used for more streamlined geometries for active boundary layer control, such as in critical components of the outer-body shell of automobiles or aircraft, near the points of separation. Strategically reducing the overall aerodynamic drag of these structures could potentially lead to enhanced fuel efficiency; a timely priority for the automotive and aircraft industries.[17]

Experimental Section

Fabrication of Samples: We used a combination of rapid prototyping, coating and casting to fabricate our samples, which enabled systematic experimentation through the fine-tuning of the geometrical and material design parameters (see Figure S1). By using a variety of silicone-based polymers – Polydimethylsiloxane, Ecoflex and Vinylpolysiloxane (see Table S1)—we explored the Young's moduli ratio in the range $9 \leq E_f / E_s \leq 162$, between the film and substrate, respectively. The outer thin shells were manufactured by first hot-vacuum forming hemispherical molds out of Polystyrene sheets and then coating them similarly to the Landau-Levich method,[29] albeit on a curved surface. During coating, by controlling the viscosity and curing time of the polymer, the gravity-induced drainage yielded thin shells of constant thickness (within ~10%) in the range $20 < h[\mu m] < 1000$. The inner soft substrate containing an inner cavity was then cast using a laser-cut and 3D-printed scaffold. Upon demolding, each sample was homogeneously compressed by depressurizing the inner cavity using a pneumatic system connected to a vacuum pump. More details on the coating and curing protocols, as well as the materials used are provided in the Supporting Information.

Surface Profilometry: The topography of the resulting wrinkling patterns was digitized using a 3D laser scanner and the data was post-processed using an in-house Matlab code to quantify the wavelength and roughness of the pattern (see Supporting Information).

Wind Tunnel Testing: For the wind tunnel tests, two identical hemispherical Smorphs were attached by a 3D-printed annulus at their equator. Finally, the resulting spherical sample was mounted onto a custom load cell, downstream, which simultaneously allowed for pneumatic depressurization and measurement of the aerodynamic drag force on the Smorphs under wind loading, for different flow conditions (see Supporting Information).

Supporting Information

Supporting Information is available from the Wiley Online Library or from the author.

[1] K.-H. Chu, R. Enright, E. N. Wang, *Appl. Phys. Lett.* **2012**, *100*, 241603–241603.
[2] D.-Y. Khang, H. Jiang, Y. Huang, J. A. Rogers, *Science* **2006**, *311*, 208–212.
[3] E. P. Chan, A. J. Crosby, *Adv. Mater.* **2006**, *18*, 3238–3242.
[4] P.-C. Lin, S. Yang, *Soft Matter* **2009**, *5*, 1011–1018.
[5] P. Ball, *Nature* **1999**, *400*, 507.
[6] S. Talley, G. Mungal, *NASA Ames/Stanford University* **2002**, 363–376.
[7] P. W. Bearman, J. K. Harvey, *Aeronaut. Quat.* **1976**, *27*, 112–122.
[8] R. D. Mehta, *Annu. Rev. Fluid. Mech.* **1985**, *17*, 151–189.
[9] G. Arthur, B. McKeon, S. Dearing, J. Morrison, Z. Cui, *Microelectron. Eng.* **2006**, *83*, 1205–1208.
[10] C.-M. Ho, Y.-C. Tai, *Annu. Rev. Fluid. Mech.* **1998**, *30*, 579–612.
[11] K.-S. Choi, T. Jukes, R. Whalley, *Philos. T. R. Soc. A* **2011**, *36*, 1443–1458.
[12] S. S. Dearing, J. F. Morrison, L. Iannucci, *Sensor. Actuat. A-phys.* **2010**, *157*, 210–218.
[13] N. Bowden, S. Brittain, A. G. Evans, J. W. Hutchinson, G. M. Whitesides, *Nature* **1998**, *393*, 146–149.
[14] X. Chen, J. W. Hutchinson, *J. Appl. Mech.* **2004**, *71*, 597–603.
[15] B. Audoly, A. Boudaoud, *J. Mech. Phys. Solids.* **2008**, *56*, 2401–2421.
[16] J. Yin, J. L. Yagüe, D. Eggenspieler, K. K. Gleason, M. C. Boyce, *Adv. Mater.* **2012**, *24*, 5441–5446.
[17] B. Richter, D. Goldston, G. Crabtree, L. Glicksman, D. Goldstein, D. Greene, D. Kammen, M. Levine, M. Lubell, M. Savitz, D. Sperling, F. Schlachter, J. Scofield, J. Dawson, *Rev. Mod. Phys.* **2008**, *80*, S1.
[18] E. Achenbach, *J. Fluid. Mech.* **1972**, *54*, 565–575.
[19] E. Achenbach, *J. Fluid. Mech.* **1974**, *65*, 113–125.
[20] E. Achenbach, *J. Fluid. Mech.* **1971**, *46*, 321–335.
[21] D. Breid, A. J. Crosby, *Soft Matter* **2013**, *9*, 3624–3630.
[22] H. G. Allen, *Analysis and design of structural sandwich panels*, Pergamon, New York, USA **1969**.
[23] S. Cai, D. Breid, A. J. Crosby, Z. Suo, J. W. Hutchinson, *J. Mech. Phys. Solids.* **2011**, *59*, 1094–1114.
[24] G. Cao, X. Chen, C. Li, A. Ji, Z. Cao, *Phys. Rev. Lett.* **2008**, *100*, 036102.
[25] B. Li, F. Jia,, Y.-P. Cao, X.-Q. Feng, H. Gao, *Phys. Rev. Lett.* **2011**, *106*, 234301.
[26] L. Prandtl, *Verhandlungen des dritten internationalen Mathematiker-Kongresses in Heidelberg : vom 8. bis 13. august 1904*, (Ed: A. Krazer), Leipzig: B. G. Teubner, Germany **1905**, p. 484.
[27] P. W. Bearman, J. K. Harvey, *AIAA. J.* **1993**, *31*, 1753–1756.
[28] H. Choi, W.-P. Jeon, J. Kim, *Annu. Rev. Fluid. Mech.* **2008**, *40*, 113–139.
[29] L. Landau, B. Levich, *Acta Physicochim. Urs.* **1942**, *17*, 42–54.
[30] F. Brau, H. Vandeparre, A. sabbah, C. Poulard, A. Boudaoud, P. Damman, *Nature Phys.* **2011**, *7*, 56–60.
[31] A. N. Gent, *Engineering with Rubber: How to Design Rubber Components*, Hanser Publications **2001**.